

1

Comparison of Terrain Following and Cut Cell Grids using a 2 Non-Hydrostatic Model

3 James Shaw* and Hilary Weller

4 *Department of Meteorology, University of Reading, Reading, United Kingdom*

5 *Corresponding author address: Department of Meteorology, University of Reading, Earley Gate,
6 PO Box 243, Reading, RG6 6BB, UK.
7 E-mail: js102@zepler.net

ABSTRACT

8 Terrain following coordinates are widely used in operational models but the
9 cut cell method has been proposed as an alternative that can more accurately
10 represent atmospheric dynamics over steep orography. Because the type of
11 grid is usually chosen during model implementation, it is typically neces-
12 sary to use different models in order to compare the accuracy of different
13 grids. In contrast, here a single C-grid finite volume model is used to en-
14 able a like-for-like comparison of terrain following and cut cell grids. A se-
15 ries of standard two-dimensional tests using idealised terrain are performed:
16 tracer advection in a prescribed horizontal velocity field, a test starting from
17 stably stratified initial conditions, and orographically induced gravity waves
18 described by nonhydrostatic dynamics. In addition, two new tracer advection
19 tests are formulated having a velocity field that is everywhere tangential to
20 the terrain following coordinate surfaces. These new tests present a challenge
21 to the advection scheme on cut cell grids. The results of the advection tests
22 demonstrate that tracer accuracy depends upon alignment of the flow with the
rather than depending on the grid uniformity or orthogonality
23 grid. As expected, the cut cell grid maintains greater accuracy for horizontal
24 advection and in the test of stationary, stratified flow. In the gravity waves
25 test, results on all grids are in good agreement with existing results from the
26 literature, although terrain following velocity fields lead to errors on cut cell
27 grids.

Somewhere in the abstract you should say: Due to careful cut-cell construction, semi-implicit time-stepp

28 **1. Introduction**

29 Representing orography accurately in numerical weather prediction systems is necessary to
30 model downslope winds and local precipitation. Orography also exerts strong non-local influences:
31 from the latent heat release due to convection, by directly forcing gravity waves and planetary waves,
32 and by the atmospheric response to form drag and gravity wave drag. There are
33 two main approaches to representing orography on a grid: terrain following layers and cut cells,
34 with the immersed (or embedded) boundary method (Simon et al. 2012) being similar to a cut cell
35 approach. All methods align cells in vertical columns. Because most models are designed for a
36 particular type of grid, existing studies of cut cell solutions have compared results with terrain
37 following grid solutions implemented within different models, for example Good et al. (2014). Instead,
38 this study uses a single model to enable a like-for-like comparison between solutions using
39 terrain following and cut cell grids.

This sounds as if you are aware of other

40 With increasing horizontal model resolution, the discrete representation of terrain can become
41 steeper, making accurate calculation of the horizontal pressure gradient more difficult when using
42 terrain following layers (Gary 1973; Steppeler et al. 2002). Numerical errors in this calculation
43 result in spurious winds and can cause numerical instability (Fast 2003; Webster et al. 2003). Cut
44 cell methods seek to reduce the error that is associated with steep orography.

45 With terrain following (TF) layers the terrain's influence decays with height so that the bottommost
46 layers follow the underlying surface closely while the uppermost layers are flat. There
47 are two main approaches to minimizing errors associated with TF layers. First, by smoothing
48 the effects of terrain with height, the influence of the terrain is reduced, hence errors in the calculated
49 horizontal pressure gradient are also reduced aloft (Schär et al. 2002; Leuenberger et al.

50 2010; Klemp 2011). However, the error is not reduced at the ground where steep terrain remains
51 unmodified.

52 Second, numerical errors can also be reduced by improving the accuracy in calculating the hor-
53 izontal pressure gradient itself. TF layers are usually implemented using a coordinate transforma-
54 tion onto a rectangular computational domain, which introduces metric terms into the equations of
55 motion. The techniques proposed by Klemp (2011) and Zängl (2012) both involve interpolation
56 onto z -levels in order to calculate the horizontal pressure gradient. This gave them the flexibility to
57 design more accurate horizontal pressure gradient discretizations using more appropriate stencils.

58 The technique proposed by Weller and Shahrokh (2014) involved calculating pressure gradients only in 1
Despite their associated numerical errors, TT layers are in widespread operational use (Step-

59 peler et al. 2003). They are attractive because their rectangular structure is simple to process by
60 computer and link with parameterisations, and boundary layer resolution can be increased with
61 variable spacing of vertical layers (Schär et al. 2002).

62 Cut cells is an alternative method in which the grid does not follow the terrain but, instead, cells
63 that lie entirely below the terrain are removed, and those that intersect the surface are modified in
64 shape so that they more closely fit the terrain. The resulting grid is orthogonal everywhere except
65 near cells that have been cut. Hence, errors are still introduced when calculating the horizontal
66 pressure gradient between cut and uncut cells.

67 The cut cell method can create some very small cells which reduce computational efficiency
68 (Klein et al. 2009), and several approaches have been tried to alleviate the problem. Yamazaki
69 and Satomura (2010) combine small cells with horizontally or vertically adjacent cells. Steppeler
70 et al. (2002) employ a thin-wall appoximation to increase the computational volume of small cells
71 without altering the terrain. Jebens et al. (2011) avoid the timestep restriction associated with
72 explicit schemes by using an implicit method for cut cells and a semi-explicit method elsewhere.

73 Several studies have shown examples where cut cells produce more accurate results when com-
74 pared to TF coordinates. Spurious winds seen in TF coordinates are not present with cut cells and
75 errors do not increase with steeper terrain (Good et al. 2014). A comparison of TF and cut cells
76 using real initial data by Steppeler et al. (2013) found that five-day forecasts of precipitation and
77 wind over Asia in January 1989 were more accurate in the cut cell model, although this result was
78 dependent on using an old version of a model. **Two is not several. Any more?**

79 Another alternative method is the eta coordinate, described by Mesinger et al. (1988). This
80 transformation, expressed in pressure coordinates, quantises the surface pressure at each grid box
81 using prescribed geometric heights. This results in terrain profiles having a staircase pattern which
82 is known as ‘step’ orography. The eta coordinate improves the accuracy of the horizontal pressure
83 gradient calculation compared to the sigma coordinate (Mesinger et al. 1988).

84 In an experiment of orographically induced gravity waves, Gallus and Klemp (2000) found that
85 horizontal flow along the lee slope was artificially weak in the Eta model. Mesinger et al. (2012)
86 offer an explanation for this behaviour: air flowing along the lee slope cannot travel diagonally
87 downwards but must first travel horizontally, then vertically downward. However, lee slope winds
88 are weakened because some of the air continues to be transported horizontally aloft.

89 Mesinger et al. (2012) refined the formulation to allow diagonal transport of momentum and
90 temperature immediately above sloping terrain. This arrangement is similar to the finite volume
91 cut cell method. The new method improved test results, increasing lee slope winds by 4 m s^{-1} to
92 5 m s^{-1} (Mesinger et al. 2012).

93 This study uses a modified version of the fully-compressible model from Weller and Shahrokhi
94 (2014) to enable a like-for-like comparison between terrain following and cut cell grids for ide-
95 alised, two-dimensional test cases from the literature. Section 2 presents the formulation of the
96 terrain following and cut cell grids used in the experiments that follow. In section 3 we give the

97 governing equations, outline the model from Weller and Shahrokhi (2014) and describe the mod-
98 ification which improves stability for long timesteps in the presence of steep orography. Section
99 4 analyses the results from three tracer advection tests, a test of a stably stratified atmosphere ini-
100 tially at rest, and orographically induced gravity waves. Concluding remarks are made in section
101 5.

102 2. Grids

103 Here we describe the formulation of the terrain following grids and the method of cut cell grid
104 construction. The techniques presented are used to define the grids for the experiments in the
105 subsequent section.

106 Gal-Chen and Somerville (1975) proposed a basic terrain following (BTF) coordinate defined
107 as

$$z = (H - h)(z^*/H) + h \quad (1)$$

108 where, in two dimensions, $z(x, z^*)$ is the physical height of the Cartesian coordinate surface at the
109 model level with transformed height z^* , H is the height of the domain, and $h(x)$ is the height of
110 the terrain surface. In this formulation z varies between h and H and z^* ranges from 0 to H . Using
111 this coordinate, the terrain's influence decays linearly with height but disappears only at the top of
112 the domain. An example is shown in figure 1a.

113 The smooth level vertical (SLEVE) coordinate proposed by Schär et al. (2002) achieves a more
114 regular TF grid in the middle and top of the domain than the BTF coordinate. The terrain height
115 is split into large-scale and small-scale components, h_1 and h_2 , such that $h = h_1 + h_2$, with each
116 component having a different exponential decay. The transformation is defined as

$$z = z^* + h_1 b_1 + h_2 b_2 \quad (2)$$

¹¹⁷ where the vertical decay functions are given by

$$b_i = \frac{\sinh((H/s_i)^n - (z^*/s_i)^n)}{\sinh(H/s_i)^n} \quad (3)$$

¹¹⁸ with s_1 and s_2 are the scale heights of large-scale and small-scale terrain respectively. The exponent
¹¹⁹ n was introduced by Leuenberger et al. (2010) in order to increase cell thickness in the layers
¹²⁰ nearest the ground, allowing longer timesteps. Leuenberger et al. (2010) found the exponent has
¹²¹ an optimal value of $n = 1.35$. Choosing $n = 1$ gives the decay functions used by Schär et al.
¹²² (2002). An example of the SLEVE grid can be seen in figure 1b.

¹²³ Most implementations of terrain following layers use a coordinate system that makes the com-
¹²⁴ putational domain rectangular, but introduces metric terms into the equations of motion. Instead,
¹²⁵ the model employed in this study uses Cartesian coordinates and non-orthogonal grids. By doing
¹²⁶ so, results from the same model can be compared between terrain following and cut cell grids
¹²⁷ without modifying the equation set or discretisation.

¹²⁸ The OpenFOAM utility `snappyHexMesh` was used to create grids that approximate the cut cell
¹²⁹ method. The utility intersects the surface faces from the BTF grid with a rectangular grid, remov-
¹³⁰ ~~i~~Cut-cell grids were created, starting from a uniform grid and then moving all cell vertices lying underneat
¹³¹ vertices so that they are ‘snapped’ to the BTF surface (OpenCFD Foundation cited 2015). The
¹³² grid that `snappyHexMesh` accepts as input is generated by a custom utility so that `snappyHexMesh`
¹³³ performs fewer, smaller vertex displacements, resulting in grids that are closer to those produced
¹³⁴ by typical shaving methods, as described by Adcroft et al. (1997).

¹³⁵ There are two details of grid construction which mean that resulting cut cell grids can differ
¹³⁶ If you use the no snapping approach, I don't think that you need to mention `snappyHexMesh`. You are

¹³⁷ slightly off. First, it does not move points horizontally to lie on the surface. Second, it does not create new
¹³⁸ points necessary for pentagonal cells. An example of these effects is shown in figure 2 in which vertex v has been

¹³⁹ moved vertically and horizontally to avoid creating a small cell. The resultant mesh, shown by
¹⁴⁰ thick dashed lines, contains triangular and quadrangular cells. With a typical shaving method,
¹⁴¹ cell c would be pentagonal, as shown by the dotted line. However, snappyHexMesh creates a
¹⁴² quadrilateral cell.

¹⁴³ 3. Models

¹⁴⁴ Three models are used for the test cases in this study: two linear advection models and a model
¹⁴⁵ of the fully-compressible Euler equations. All are operated in a two-dimensional $x-z$ slice config-
¹⁴⁶ uration.

¹⁴⁷ The two finite volume models make use of the upwind-biased multidimensional cubic advection
¹⁴⁸ scheme from Weller and Shahrokhi (2014) which is non-monotonic and not flux corrected. The
¹⁴⁹ scheme uses a least squares fit of a multidimensional polynomial using an upwind-biased stencil.

¹⁵⁰ ~~Weightings are iteratively adjusted in the least squares fit procedure to ensure that advection re-~~
¹⁵¹ ~~mains upwind-biased where the stencil includes small cut cells. *TODO: I can see reviewers saying*~~
¹⁵² ~~*that this isn't a sufficiently detailed explanation...?*~~ See replacement text

Put the description of the advection scheme in section 3a

¹⁵³ a. Finite volume linear advection model

¹⁵⁴ The first model discretises the linear advection equation in flux form:

$$\partial\phi/\partial t + \nabla \cdot (\mathbf{u}\phi) = 0 \quad (4)$$

¹⁵⁵ where $\mathbf{u} = (u, w)$ is a prescribed velocity field and the tracer density, ϕ , is interpolated onto cell
¹⁵⁶ faces using one of two schemes: first, the centred linear scheme which takes the average of the two
¹⁵⁷ neighbouring cell values; second, the upwind-biased cubic scheme. The time derivative is solved

¹⁵⁸ using a three-stage, second order Runge-Kutta scheme defined as:

$$\phi^* = \phi^{(n)} + \Delta t f(\phi^{(n)}) \quad (5a)$$

$$\phi^{**} = \phi^{(n)} + \frac{\Delta t}{2} \left(f(\phi^{(n)}) + f(\phi^*) \right) \quad (5b)$$

$$\phi^{(n+1)} = \phi^{(n)} + \frac{\Delta t}{2} \left(f(\phi^{(n)}) + f(\phi^{**}) \right) \quad (5c)$$

¹⁵⁹ where $f(\phi^{(n)}) = -\nabla \cdot (\mathbf{u}\phi^{(n)})$ at time level n . This time-stepping scheme is used for consistency
¹⁶⁰ with the trapezoidal implicit scheme used for the fully-compressible model, described in sec-
¹⁶¹ tion 3c. To ensure that the discrete velocity field is non-divergent, velocities are prescribed at cell
¹⁶² faces by differencing the streamfunction, $\Psi(x, z)$, along the edges from Ψ stored at cell vertices.

¹⁶³ b. Finite difference linear advection model

¹⁶⁴ The second model is a modified version of the linear advection model first used by Schär et al.
¹⁶⁵ (2002). It uses terrain following coordinates and it is configured with leapfrog timestepping and
¹⁶⁶ either second-order centred differences, or a fourth-order centred difference scheme given by:

$$\frac{\partial \phi_i}{\partial x} \approx \frac{1}{\Delta x} \left(\frac{1}{12} \phi_{i-2} - \frac{2}{3} \phi_{i-1} + \frac{2}{3} \phi_{i+1} - \frac{1}{12} \phi_{i+2} \right) \quad (6)$$

¹⁶⁷ and similarly for $\partial \phi_i / \partial z$.

¹⁶⁸ Once again, velocity fields are prescribed using a streamfunction defined at cell vertices (referred
¹⁶⁹ to as double staggered grid points by Schär et al. (2002)). The original version of the code effec-
¹⁷⁰ tively smoothed the orography, interpolating the geometric height, z , at doubly staggered points
¹⁷¹ from values at adjacent half levels in order to calculate the streamfunction. The modified version
¹⁷² used here directly calculates the height at vertices to enable comparisons with the finite volume
¹⁷³ model solutions.

¹⁷⁴ c. Finite volume fully-compressible model

¹⁷⁵ The third model is taken from Weller and Shahrokh (2014) which details a discretisation of the
¹⁷⁶ fully-compressible Euler equations, given by

$$\text{Momentum} \quad \frac{\partial \rho \mathbf{u}}{\partial t} + \nabla \cdot \rho \mathbf{u} \otimes \mathbf{u} = \rho \mathbf{g} - c_p \rho \theta \nabla \Pi - \mu \rho \mathbf{u} \quad (7a)$$

$$\text{Continuity} \quad \frac{\partial \rho}{\partial t} + \nabla \cdot \rho \mathbf{u} = 0 \quad (7b)$$

$$\text{Thermodynamic equation} \quad \frac{\partial \rho \theta}{\partial t} + \nabla \cdot \rho \mathbf{u} \theta = 0 \quad (7c)$$

$$\text{Ideal gas law} \quad \Pi^{(1-\kappa)/\kappa} = \frac{R\rho\theta}{p_0} \quad (7d)$$

where ρ is the density, \mathbf{u} is the velocity field, \mathbf{g} is the gravitational acceleration, c_p is the heat capacity at constant pressure, $\theta = T(p_0/p)^\kappa$ is the potential temperature, T is the temperature, p is the pressure, p_0 is a reference pressure, $\Pi = (p/p_0)^\kappa$ is the Exner function of pressure, and $\kappa = R/c_p$ is the gas constant to heat capacity ratio. μ is a dimensionless damping function used for the sponge layer in the gravity waves test in section 4d.

The fully-compressible model uses the C-grid staggering in the horizontal and the Lorenz staggering in the vertical such that θ , ρ and Π are stored at cell centroids and the covariant component of velocity at cell faces. The model is configured without Coriolis forces.

185 Acoustic and gravity waves are treated implicitly and advection is treated explicitly. The trape-
 186 zoidal implicit treatment of fast waves and the Hodge operator suitable for non-orthogonal grids
 187 are described in appendix A. To avoid time-splitting errors between the advection and the fast
 188 waves, the advection is time-stepped using a three-stage, second-order Runge-Kutta scheme. The
 189 advection terms of the momentum and θ equations, (7a) and (7c), are discretised in flux form
 190 using the upwind-biased cubic scheme.

191 **4. Results**

192 A series of two-dimensional tests are performed over idealised orography. For each test, results
193 on terrain following and cut cell grids are compared. The first test from Schär et al. (2002) advects
194 a tracer in a horizontal velocity field. Second, a new tracer advection test is formulated employing
195 a terrain following velocity field to challenge the advection scheme on cut cell grids. The third
196 test solves the Euler equations for a stably stratified atmosphere initially at rest, following Klemp
197 (2011). Fourth, as specified by Schär et al. (2002), a test of orographically-induced gravity waves
198 is performed. Finally, another tracer advection test is formulated that transports a stably stratified
199 thermal profile in a terrain following velocity field. No explicit diffusion is used in any of the tests.

200 The OpenFOAM implementation of the numerical model, grid generation utilities and test
201 cases are available at <https://github.com/hertzprung/tf-cutcell-comparison/tree/>
202 shaw-weller-2015-mwr.

203 *a. Horizontal advection*

204 Following Schär et al. (2002), a tracer is transported above wave-shaped terrain by solving the
205 advection equation for a prescribed horizontal wind. This test challenges the accuracy of the
206 advection scheme in the presence of grid distortions.

207 The domain is 301 km wide and 25 km high, discretized onto a grid with $\Delta x = 1 \text{ km}$ and $\Delta z^* =$
208 500 m. The domain specified by Schär et al. (2002) is 300 km between the outermost cell centres
209 where tracer values are specified. In order to reproduce the result from Schär et al. (2002), the
210 domain has been extended horizontally by $\Delta x/2 \text{ m}$ in both directions so that the distance between
211 the outermost cell centres is still 300 km.

²¹² The terrain is wave-shaped, specified by the surface height, h , such that

$$h(x) = h^* \cos^2(\alpha x) \quad (8a)$$

²¹³ where

$$h^*(x) = \begin{cases} h_0 \cos^2(\beta x) & \text{if } |x| < a \\ 0 & \text{otherwise} \end{cases} \quad (8b)$$

²¹⁴ where $a = 25$ km is the mountain envelope half-width, $h_0 = 3$ km is the maximum mountain height,
²¹⁵ $\lambda = 8$ km is the wavelength, $\alpha = \pi/\lambda$ and $\beta = \pi/(2a)$. On the SLEVE grid, the large-scale
²¹⁶ component h_1 is given by $h_1(x) = h^*(x)/2$ and $s_1 = 15$ km is the large scale height, and $s_2 = 2.5$ km
²¹⁷ is the small scale height. The optimisation of SLEVE by Leuenberger et al. (2010) is not used, so
²¹⁸ the exponent $n = 1$.

²¹⁹ The wind is entirely horizontal and is prescribed as

$$u(z) = u_0 \begin{cases} 1 & \text{if } z \geq z_2 \\ \sin^2\left(\frac{\pi}{2} \frac{z-z_1}{z_2-z_1}\right) & \text{if } z_1 < z < z_2 \\ 0 & \text{otherwise} \end{cases} \quad (9)$$

²²⁰ where $u_0 = 10$ m s⁻¹, $z_1 = 4$ km and $z_2 = 5$ km. This results in a constant wind above z_2 , and zero
²²¹ flow at 4 km and below.

²²² The discrete velocity field is defined using a streamfunction, Ψ . Given that $u = -\partial\Psi/\partial z$, the
²²³ streamfunction is found by vertical integration of the velocity profile:

$$\Psi(z) = -\frac{u_0}{2} \begin{cases} (2z - z_1 - z_2) & \text{if } z > z_2 \\ z - z_1 - \frac{z_2 - z_1}{\pi} \sin\left(\pi \frac{z-z_1}{z_2-z_1}\right) & \text{if } z_1 < z \leq z_2 \\ 0 & \text{if } z \leq z_1 \end{cases} \quad (10)$$

224 A tracer with density ϕ is positioned upstream above the height of the terrain. It has the shape

$$\phi(x, z) = \phi_0 \begin{cases} \cos^2\left(\frac{\pi r}{2}\right) & \text{if } r \leq 1 \\ 0 & \text{otherwise} \end{cases} \quad (11)$$

225 having radius, r , given by

$$r = \sqrt{\left(\frac{x-x_0}{A_x}\right)^2 + \left(\frac{z-z_0}{A_z}\right)^2} \quad (12)$$

226 where $A_x = 25\text{ km}$, $A_z = 3\text{ km}$ are the horizontal and vertical half-widths respectively, and $\phi_0 = 1$
227 is the maximum density of the tracer. At $t = 0\text{ s}$, the tracer is centred at $(x_0, z_0) = (-50\text{ km}, 9\text{ km})$
228 so that the tracer is upwind of the mountain and well above the maximum terrain height of 3 km.

229 Analytic solutions can be found by setting the tracer centre such that $x_0 = ut$. Unlike Schär et al.
230 (2002) who use periodic lateral boundaries, a fixed value of 0 is used at the inlet boundary and
231 all other boundaries have zero gradient. Furthermore, a second order Runge-Kutta timestepping
232 scheme is used here instead of the leapfrog scheme used by Schär et al. (2002). Tests are integrated
233 forward in time for 10 000 s with a timestep of $\Delta t = 25\text{ s}$.

234 The test was executed on the BTF, SLEVE and cut cell grids, and on a regular grid with flat
235 terrain using a centred linear scheme and the upwind-biased cubic scheme. Results were also
236 obtained on BTF and SLEVE grids with the fourth order scheme from Schär et al. (2002) using
237 the modified version of their code.

238 Tracer contours at $t = 0\text{ s}$, 5000 s and 10 000 s are shown in Figure 3. The results are compared
239 on the BTF grid for the centred linear scheme (3a) and the fourth order scheme from Schär et al.
240 (2002) (3c), and the upwind-biased cubic scheme on the cut cell grid (3b), and BTF grid (3d).
241 Tracer errors at $t = 10 000\text{ s}$ are shown for the fourth order and upwind-biased cubic schemes in
242 figures 3e and 3f respectively.

243 By $t = 10\,000$ s, the tracer suffers from distortion on the BTF grid using the centred linear scheme
 244 and some artifacts remain about the mountain peak. The results are visually identical to those using
 245 the modified Schär model with centred linear differencing. The tracer has spread vertically due to
 246 increased numerical errors when the tracer is transported between layers. Distortions are reduced
 247 by using the fourth order scheme from Schär et al. (2002) (figure 3c), but dispersion errors remain
 248 with grid-scale oscillations that travel in the opposite direction to the wind (figure 3e). The results
 249 from the centred linear and fourth order schemes are slightly worse than the respective results from
 250 Schär et al. (2002) (their figure 6a and figure 8) because of the difference in the discretisation of
 251 the streamfunction, Ψ .

252 Using the upwind-biased cubic scheme, tracer magnitude and shape are well-preserved on all
 253 grids, both above the mountain at $t = 5000$ s and past the mountain at $t = 10\,000$ s. In this test,
 254 advection is most accurate on the cut cell grid (figure 3b) and regular grid (not shown). As found
 255 by Good et al. (2014), the result is the same on both grids. This is to be expected since the wind
 256 is zero in the region of the ground and flow aloft is aligned with the grids. On the BTF grid, the
 257 tracer is less distorted by the cubic upwind-biased scheme (figure 3d) compared to the centred
 258 linear scheme (figure 3a) or fourth order scheme (figure 3c).

259 Minimum and maximum tracer values and ℓ_2 error norms on the BTF, SLEVE, cut cell and
 260 regular grids are summarised in table 1, where the ℓ_2 error norm is defined as

$$\ell_2 = \sqrt{\frac{\sum_c (\phi - \phi_T)^2 \mathcal{V}_c}{\sum_c (\phi_T^2 \mathcal{V}_c)}} \quad (13)$$

261 where ϕ is the numerical tracer value, ϕ_T is the analytic value and \mathcal{V}_c is the cell volume.

262 The results of the cubic upwind-biased scheme on TF and regular grids are comparable with
 263 those for the fourth-order centred scheme from Schär et al. (2002). Error is largest on the BTF
 264 grid with $\ell_2 = 0.107$ but is significantly reduced on the SLEVE grid with $\ell_2 = 0.0146$. The error

265 is approximately halved by changing from the SLEVE grid to the cut cell grid. Tracer minima and
266 maxima for the centred linear and fourth order schemes are lower than those presented by Schär
267 et al. (2002) because no interpolation is used to calculate the streamfunction.

268 The centred linear scheme is sensitive to grid-scale changes in the terrain profile: when the
269 domain width is reduced to 300 km, the ℓ_2 error on the BTF grid rises from 0.284 to 0.432. The
270 same sensitivity is found using terrain following coordinates and centred differences in space and
271 time, as implemented by Schär et al. (2002). The upwind-biased cubic scheme is less sensitive
272 to the same change, with the ℓ_2 error decreasing from 0.107 to 0.104. It is likely that changes
273 in the domain width affect the wave power spectrum of the discrete terrain profile. Grid-scale
274 oscillations persist in the centred linear scheme but are damped by the upwind-biased scheme.

275 The results of the horizontal advection test show that numerical errors are due either to mis-
276 alignment of the flow with the grid, or to grid distortions. Using the upwind-biased cubic scheme,
277 distortions in the grid do not significantly distort the tracer.

278 *b. Terrain following advection*

279 In the horizontal advection test, results were least accurate on the BTF grid, where the grid
280 was most non-orthogonal and flow was misaligned with the grid layers. Here, we formulate a
281 new tracer advection test in which the velocity field is everywhere tangential to the basic terrain
282 following coordinate surfaces. This test determines whether the primary source of numerical error
283 is due to non-orthogonality or misalignment of the flow with grid layers.

284 The spatial domain, mountain profile, initial tracer profile and discretisation are the same as
285 those in the horizontal tracer advection test. The velocity field is defined using a streamfunction,
286 Ψ , so that the discrete velocity field is non-divergent and follows the BTF coordinate surfaces

287 given by equation 1 such that

$$\Psi(x, z) = -u_0 H \frac{z - h}{H - h} \quad (14)$$

288 where $u_0 = 10 \text{ m s}^{-1}$, which is the horizontal wind speed where $h(x) = 0$. The horizontal and
289 vertical components of velocity, u and w , are then given by

$$u = -\frac{\partial \Psi}{\partial z} = u_0 \frac{H}{H - h}, \quad w = \frac{\partial \Psi}{\partial x} = u_0 H \frac{dh}{dx} \frac{H - z}{(H - h)^2} \quad (15)$$

$$\frac{dh}{dx} = -h_0 [\beta \cos^2(\alpha x) \sin(2\beta x) + \alpha \cos^2(\beta x) \sin(2\alpha x)] \quad (16)$$

290 Unlike the horizontal advection test, flow extends from the top of the domain all the way to the
291 ground. The discrete velocity field is calculated using the streamfunction in the same way as the
292 horizontal advection test.

293 At $t = 10000 \text{ s}$ the tracer has passed over the mountain. The horizontal position of the tracer
294 centre can be calculated by integrating along the trajectory to find t , the time taken to pass from
295 one side of the mountain to the other:

$$dt = dx/u(x) \quad (17)$$

$$t = \int_0^x \frac{H - h(x)}{u_0 H} dx \quad (18)$$

$$t = \frac{x}{u_0} - \frac{h_0}{16u_0 H} \left[4x + \frac{\sin 2(\alpha + \beta)x}{\alpha + \beta} + \frac{\sin 2(\alpha - \beta)x}{\alpha - \beta} + 2 \left(\frac{\sin 2\alpha x}{\alpha} + \frac{\sin 2\beta x}{\beta} \right) \right] \quad (19)$$

296 Hence, we find that $x(t = 10000 \text{ s}) = 51577.4 \text{ m}$. Because the velocity field is non-divergent,
297 the flow accelerates over mountain ridges and the tracer travels 1577.4 m further compared to
298 advection in the purely horizontal velocity field. Tracer height is unchanged downwind of the
299 mountains because advection is along the terrain following coordinate surface.

300 ℓ_2 errors and tracer extrema for this test are compared with the horizontal advection results in
301 table 1. In the terrain following velocity field, tracer accuracy is greatest on the BTF grid. Using

302 the cubic upwind-biased scheme, errors are about ten times larger on the SLEVE and cut cell grids
303 compared to the BTF grid.

304 Using the centred linear scheme on the cut cell grid, numerical instability is generated by flow
305 through small cells: when interpolating ϕ onto faces, flux from a large cell into a small cell means
306 that the downwind cell is given greater weighting, effectively making the scheme downwind-
307 biased rather than upwind-biased. The maximum Courant number is less than one in all of the
308 advection tests, hence it is not the source of this instability.

309 We conclude from this test that accuracy depends upon alignment of the flow with the grid, and
310 accuracy is not significantly reduced by grid distortions. Error on the BTF grid in the terrain fol-
311 lowing advection test is comparable with the error on the SLEVE grid in the horizontal advection
312 test.

313 *c. Stratified atmosphere initially at rest*

314 An idealised terrain profile is defined along with a stably stratified atmosphere at rest in hy-
315 drostatic balance. The analytic solution is time-invariant, but numerical errors in calculating the
316 horizontal pressure gradient can give rise to spurious velocities which become more severe over
317 steeper terrain (Klemp 2011).

318 The test setup follows the specification by Klemp (2011). The domain is 200 km wide and 20 km
319 high, and the grid resolution is $\Delta x = \Delta z^* = 500$ m. All boundary conditions are no normal flow.

320 The wave-shaped mountain profile has a surface height, h , given by

$$h(x) = h_0 \exp\left(-\left(\frac{x}{a}\right)^2\right) \cos^2(\alpha x) \quad (20)$$

321 where $a = 5$ km is the mountain half-width, $h_0 = 1$ km is the maximum mountain height and
322 $\lambda = 4$ km is the wavelength. For the optimised SLEVE grid, the large-scale component h_1 is

323 specified as

$$h_1(x) = \frac{1}{2}h_0 \exp\left(-\left(\frac{x}{a}\right)^2\right) \quad (21)$$

324 and, following Leuenberger et al. (2010), $s_1 = 4\text{ km}$ is the large scale height, $s_2 = 1\text{ km}$ is the small
325 scale height, and the optimal exponent value of $n = 1.35$ is used.

in the vertical direction

326 The initial thermodynamic conditions are in discrete hydrostatic balance, having a reference
327 potential temperature of $\theta(z = 0) = 288\text{ K}$ and constant stability with Brunt-Väisälä frequency
328 $N = 0.01\text{ s}^{-1}$ everywhere, except for a more stable layer of $N = 0.02\text{ s}^{-1}$ between $2\text{ km} \leq z \leq 3\text{ km}$.
329 The damping function, μ , is set to zero. Unlike Klemp (2011), there is no eddy diffusion in the
330 equation set.

331 The test was integrated forward by 5 hours on the BTF, SLEVE and cut cell grids, and a regular
332 grid with flat terrain. Maximum vertical velocities are presented in figure 4. In agreement with
333 Klemp (2011), vertical velocities are larger on more distorted grids. However, magnitudes are
334 smaller comparing results on the terrain following grids with those from Klemp (2011). The results
335 presented in figure 4, which use a curl-free pressure gradient, have maximum spurious values
336 of w of 0.33 m s^{-1} on the BTF grid, compared with a maximum of $\sim 7\text{ m s}^{-1}$ found by Klemp
337 (2011) using their improved horizontal pressure gradient formulation. The results in figure 4 have
338 the same maximum errors as Weller and Shahrokh (2014) but, due to the more stable split into
(described in the appendix)
339 implicitly and explicitly treated terms, the errors decay over time due to the dissipative nature of
340 the advection scheme.

341 Unlike the result from Klemp (2011), the SLEVE grid does not significantly reduce vertical
342 velocities compared to the BTF grid. However, errors are two orders of magnitude smaller on the
343 cut cell grid with vertical velocities of $\sim 1 \times 10^{-4}\text{ m s}^{-1}$. The smallest error of $\sim 1 \times 10^{-10}\text{ m s}^{-1}$
344 is found on the regular grid.

345 Good et al. (2014) found the maximum vertical velocity in their cut cell model was
346 $1 \times 10^{-12} \text{ m s}^{-1}$, which is better than any result obtained here. It is worth noting that ~~the~~ model
347 ~~by Weller and Shahrokh (2014)~~ stores values at the geometric centre of cut cells. ~~However,~~ In the
348 model used by Good et al. (2014), cell centres are in the centre of the uncut cell, resulting in the
349 centre of some cut cells being below the ground (S.-J. Lock 2014, personal communication). This
350 means that the grid is effectively regular when calculating horizontal and vertical gradients. This
351 would account for the very small velocities found by Good et al. (2014).

352 In summary, spurious velocities in the resting atmosphere test were similar on both terrain fol-
353 lowing grids, with lower errors compared to those from Klemp (2011). The maximum vertical
354 velocity was significantly decreased on the cut cell grid, so we conclude that non-orthogonality,
355 or lack of alignment of the grid with surfaces of constant gravitational potential are a significant
356 cause of numerical error in this test.

357 *d. Gravity waves*

358 The test originally specified by Schär et al. (2002) prescribes flow over terrain with small-scale
359 and large-scale undulations which induces propagating and evanescent gravity waves.

360 Following Melvin et al. (2010), the domain is 300 km wide and 30 km high. The mountain
361 profile has the same form as equation 20, but the gravity waves tests have a mountain height of
362 $h_0 = 250 \text{ m}$. As in the resting atmosphere test, $a = 5 \text{ km}$ is the mountain half-width and $\lambda = 4 \text{ km}$
363 is the wavelength.

364 A uniform horizontal wind $u = 10 \text{ m s}^{-1}$ is prescribed in the interior domain and at the inlet
365 boundary. No normal flow is imposed at the top and bottom boundaries and the velocity field has
366 a zero gradient outlet boundary condition.

367 The initial thermodynamic conditions have constant static stability with $N = 0.01 \text{ s}^{-1}$ every
368 where, such that

$$\theta(z) = \theta_0 \exp\left(\frac{N^2}{g}z\right) \quad (22)$$

369 where the temperature at $z = 0$ is $\theta_0 = 288 \text{ K}$. Potential temperature values are prescribed at the
370 inlet and upper boundary using equation 22, and a zero gradient boundary condition is applied at
371 the outlet. At the ground, fixed gradients are imposed by calculating the component of $\nabla\theta$ normal
372 to each face using the vertical derivative of equation 22. For the Exner function of pressure,
373 hydrostatic balance is prescribed on top and bottom boundaries and the inlet and outlet are zero
374 normal gradient.

375 Sponge layers are added to the upper 10 km and leftmost 10 km at the inlet boundary to damp
376 the reflection of waves. The damping function, μ , is adapted from Melvin et al. (2010) such that

$$\mu(x, z) = \mu_{\text{upper}} + \mu_{\text{inlet}} \quad (23)$$

$$\mu_{\text{upper}}(z) = \begin{cases} \bar{\mu} \sin^2\left(\frac{\pi}{2} \frac{z-z_B}{H-z_B}\right) & \text{if } z \geq z_B \\ 0 & \text{otherwise} \end{cases} \quad (24)$$

$$\mu_{\text{inlet}}(x) = \begin{cases} \bar{\mu} \sin^2\left(\frac{\pi}{2} \frac{x_I-x}{x_I-x_0}\right) & \text{if } x < x_I \\ 0 & \text{otherwise} \end{cases} \quad (25)$$

377 where $\bar{\mu} = 1.2$ is the damping coefficient, $z_B = 20 \text{ km}$ is the bottom of the sponge layer, $H = 30 \text{ km}$
378 is the top of the domain, $x_0 = -150 \text{ km}$ is the leftmost limit of the domain and $x_I = -140 \text{ km}$ is the
379 rightmost extent of the inlet sponge layer. The sponge layer is only active on faces whose normal
380 is vertical so that it damps vertical momentum only.

381 Note that, while the domain itself is 30 km in height, for the purposes of generating BTF grids,
382 the domain height is set to 20 km because the sponge layer occupies the uppermost 10 km.

383 The simulation is integrated forward by 5 hours and the timestep, $\Delta t = 8\Delta z/300\text{s}$, is chosen
384 so that it scales linearly with spatial resolution and, following the original test specified by Schär
385 et al. (2002), $\Delta t = 8\text{s}$ when $\Delta z = 300\text{m}$. Test results are compared between the BTF and cut cell
386 grids at several resolutions. The spatial and temporal resolutions tested are shown in table 2. The
387 lowest resolution is the same as that used by Schär et al. (2002), and higher resolutions preserve
388 the same aspect ratio. The vertical resolution is chosen to test various configurations of cut cell
389 grid. At $\Delta z = 300\text{m}$, the mountain lies entirely within the lowest layer of cells, while at $\Delta z = 250\text{m}$
390 and $\Delta z = 125\text{m}$ the mountain peak is aligned with the interface between layers. With increasing
391 resolutions up to $\Delta z = 50\text{m}$, the orography intersects more layers and becomes better resolved.
392 Three of the cut cell grids are shown in figure 5 at $\Delta z = 300\text{m}$, 250m and 200m . Small cells are
393 visible on the 200m grid but, on the 250m grid, the grid generator has merged the small cells with
394 those in the layer above. Could you redo the grid in fig 5b

395 Some statistics of the grids are presented in table 3. The ratio of minimum and maximum cell
396 areas provides an indication of size of the smallest cut cells. As expected, there is almost no
397 variation in cell sizes on the BTF grids. Small cells are generated on cut cell grids at resolutions
398 finer than $\Delta z = 300\text{m}$ in which the terrain intersects grid layers. Nonorthogonality is measured
399 by the angle between the vector connecting adjacent cell centres and the normal vector of the
400 shared cell face, ranging from 0° on an orthogonal grid, to a maximum of 90° . The maximum
401 nonorthogonality is the largest value of any face. On the BTF grid, maximum nonorthogonality
402 gradually increases from 9.2° to 11.2° as increasing horizontal resolution leads to steeper terrain.
403 Maximum nonorthogonality is higher on almost all cut cell grids at about 30° . **TODO: what do**
404 *the nonortho stats mean for us? we might expected larger HPG errors with greater nonortho (and*
405 *this was indeed the case looking at max nonortho stats in the resting atmosphere, although I've*
406 *not discussed those in the paper as it stands)*

407 At $\Delta z = 300$ m, vertical velocities on the BTF and cut cell grids are visually indistinguishable
408 (not shown). They agree with the high resolution mass-conserving semi-implicit semi-Lagrangian
409 solution from Melvin et al. (2010). The initial thermal profile is subtracted from the potential
410 temperature field at the end of the integration to reveal the structure of thermal anomalies. The
411 anomalies on the BTF grid with $\Delta z = 50$ m is shown in figure 6. A vertical profile is taken at
412 $x = 50$ km, marked by the dashed line in figure 6, with results shown for the BTF grids in figure 7a
413 and on the cut cell grids in figure 7b. On all grids, potential temperature ~~increases with height due~~
414 ~~differences increase with height, i~~
~~to the presence of a gravity wave at this location.~~ Results are seen to ~~converge on all grids, with~~
415 two exceptions. First, the result on the cut cell grid with $\Delta z = 500$ m differs from results on all
416 other grids, though at this coarse resolution the mountain is poorly resolved. Second, small errors
417 are seen in the lowest layers on the cut cell grids. ~~You don't need to comment that the dz=500m solu~~

418 To summarize, results of the gravity waves test on all grids are in good agreement with the
419 reference solution from Melvin et al. (2010). The potential temperature field converges, though
420 errors are found in the lowest layers on the cut cell grids.

The source of the errors in the cut-cell meshes will be investigated further with an advection test in the foll

421 e. Terrain following advection of thermal profile

422 The potential temperature anomalies in the gravity waves test varied between terrain following
423 and cut cell grids of the same resolution. This variation may be due to differences in the wind
424 fields between grids, or errors in the advection of potential temperature, amongst other possible
425 causes. To help establish the primary source of error, a new advection test is formulated in which
426 the initial potential temperature field from the gravity waves test is used as a tracer density field. To
427 eliminate any differences in wind fields, the tracer is advected in a fixed, terrain-following velocity
428 field that mimics the flow in the gravity waves test.

429 The spatial domain, mountain profile, grid resolutions and timesteps are the same as those in the
 430 gravity waves test in section 4d. The terrain following velocity field is defined by the streamfunc-
 431 tion:

$$\Psi(x, z) = -u_0 \begin{cases} H_{\text{TF}} \frac{z-h}{H_{\text{TF}}-h} & \text{if } z \leq H_{\text{TF}} \\ z & \text{if } z > H_{\text{TF}} \end{cases} \quad (26)$$

432 where $H_{\text{TF}} = 20\text{km}$ is the level at which the terrain following layers become flat; the domain
 433 height is 30km . For $z \leq H_{\text{TF}}$, the u and w components of velocity are given by equation 15, but
 434 $h(x)$ has the same form as equation 20, hence the derivative is:

$$\frac{dh}{dx} = -h_0 \exp\left(-\left(\frac{x}{a}\right)^2\right) \left[\alpha \sin(2\alpha x) - \frac{2x}{a^2} \cos^2(\alpha x) \right] \quad (27)$$

435 For $z > H_{\text{TF}}$, $u = u_0$ and $w = 0$.

436 The initial tracer density field, ϕ , and its boundary conditions, are the same as those of the
 437 initial potential temperature field in the gravity waves test. Following the gravity waves test,
 438 the simulation is integrated forward by 18000s , by which time the tracer initially upwind of the
 439 mountain will have cleared the mountain range. Hence, the analytic solution, ϕ_T , can be found by
 440 considering the vertical displacement of the tracer profile by the terrain following velocity field.

$$\phi_T(x, z) = \phi_0 \exp\left(\frac{N^2}{g} z^*(x, z)\right) \quad (28)$$

441 where the tracer density at $z = 0$, $\phi_0 = 288$, and the transform, z^* , is given by rearranging equa-
 442 tion 1. First refer to the figures and describe what is shown in the figures

443 Errors are small on the BTF grids with a maximum error in tracer density of 0.0376 at $\Delta z =$
 444 500m and errors are 10 to 100 times smaller on higher resolution BTF grids. Errors are also
 445 small on the cut cell grids at $\Delta z = 500\text{m}$ and $\Delta z = 300\text{m}$. However, at resolutions where the
 446 terrain intersects layers of the cut cell grids, advection errors are apparent around mountain peaks,
 447 with small cells having the largest errors. These errors are advected horizontally along the lee
It would be really useful to overlay total tracer contours on figure 8

From fig 8 I am not entirely convinced that errors are only generated or apparent at mountain peaks. They see

448 side, forming stripes. Enlargements of the error field near the mountain are shown in figure 8 at
449 $\Delta z = 50\text{m}$.

450 For comparison with the potential temperature anomalies in the gravity waves test, vertical pro-
451 files of tracer density error are taken at $x = 50\text{ km}$. As seen in figure 6c, errors are negligible on
452 the BTF grids, but figure 6d reveals significant errors in the lowest layers of the cut cell grids that
453 were advected from the mountain peaks. The magnitude of error is about ten times larger than
454 the potential temperature anomalies found on the cut cell grids in the gravity waves test seen in
455 figure 6b. We offer two explanations for this difference: first, there are no restoring forces in the
456 linear advection model and, second, the wind fields in the two tests are different.

457 While the magnitude and structure of tracer error on the cut cell grids differs from potential
458 temperature anomalies in the gravity waves test, results on the BTF grids are in close agreement
459 in both tests but not on the cut cell grids. Therefore, it is likely that anomalies on the cut cell grids
460 in the gravity waves test are primarily due to errors in the advection of potential temperature.

through cut cells

461 5. Conclusions

462 We have presented a like-for-like comparison between terrain following and cut cell grids using
463 a single model. Accuracy on the BTF, SLEVE and cut cell grids was evaluated in a series of
464 two-dimensional tests.

465 Across all tests, a high degree of accuracy was achieved for all grids. Even on the highly-
466 distorted BTF grid, which has previously been found to give poor results (Schär et al. 2002; Klemp
467 2011; Good et al. 2014), errors were often small in the tests presented here. In the first two
468 tests, tracers were advected by horizontal and terrain following velocity fields. We found that the
469 accuracy of the upwind-biased cubic advection scheme depended upon alignment of the flow with
470 the grid rather than on grid distortions.

471 Spurious vertical velocities were small in the resting initial state test, reaching a maximum of
472 $\sim 0.35 \text{ m s}^{-1}$ on the BTF grid, compared to a maximum of $\sim 7 \text{ m s}^{-1}$ found by Klemp (2011). In
473 the gravity waves test, vertical velocities were in good agreement with the reference solution from
474 Melvin et al. (2010) across all grids.

475 Cut cell grids reduced errors in two of the five tests. First, in the horizontal advection test, tracer
476 accuracy on the cut cell grid was almost as good as accuracy on a regular grid with no mountain.
477 Second, in the resting atmosphere test, spurious vertical velocities were two orders of magnitude
478 smaller on the cut cell grid compared with the terrain following grids.

479 Conversely, in the first terrain following tracer advection test, errors were large on the SLEVE
480 and cut cell grids where velocities were misaligned with the grids. Errors were also large on the
481 cut cell grids in the second terrain following tracer advection test. This result suggests that, in the
482 gravity waves test, that potential temperature anomalies in the cut cell grids are primarily due to
483 advection errors.

484 The tests we have presented demonstrate the trade-off between errors in calculating pressure
485 gradient and advection terms: pressure gradient errors can be reduced by using a cut cell grid but,
486 when flow follows the terrain, advection errors are reduced using a terrain following grid.

487 The cubic upwind-biased advection scheme takes an approach for treating small cut cells that
488 differs from other existing approaches by adjusting weightings to ensure that advection remains
489 upwind-biased near small cells. The technique is already implemented in OpenFOAM and will be
490 described in a future publication.

491 Also point out that there is not small cell problem (see text in the abstract)

492 *Acknowledgments.* I am grateful to my co-supervisors John Methven and Terry Davies for their
493 valuable input, and to Christoph Schär (ETH) for his assistance in reproducing his advection test
results. The authors thank the two anonymous reviewers whose comments greatly improved this

494 manuscript. I am thankful for the NERC studentship which helped fund this work. Weller is
495 funded by NERC grant NE/H015698/1.

496 **Appendix A . Semi-implicit treatment of the Hodge operator**

497 In order to ensure curl-free pressure gradients, following Weller and Shahrokhi (2014), the co-
498 variant momentum component, that is the momentum at the cell face in the direction between cell
499 centres, is used as the prognostic variable for velocity:

$$V_f = \rho_f \mathbf{u}_f \cdot \mathbf{d}_f \quad (29)$$

500 where \mathbf{d}_f is the vector between cell centres and subscript f means “at face f ”. The contravariant
501 momentum component, that is the flux across faces, is a diagnostic variable:

$$U_f = \rho_f \mathbf{u}_f \cdot \mathbf{S}_f \quad (30)$$

502 where \mathbf{S}_f is the outward-pointing normal vector to face f with magnitude equal to the area of the
503 face. If U is the vector of all values of U_f and V is the vector of all values of V_f then we can define
504 the Hodge operator as a matrix that transforms V to U :

$$U = HV. \quad (31)$$

505 For energy conservation, Thuburn and Cotter (2012) showed that the Hodge operator must be
506 symmetric and positive definite. We define a symmetric H suitable for arbitrary 3D meshes:

$$U_f = (\rho \mathbf{u})_F \cdot \mathbf{S}_f \quad (32)$$

507 where subscript F denotes mid-point interpolation from two surrounding cell values onto face f :

$$(\rho \mathbf{u})_F = \frac{1}{2} \sum_{c \in f} (\rho \mathbf{u})_C \quad (33)$$

508 where $c \in f$ denotes the two cells sharing face f . $(\rho \mathbf{u})_C$ is the consistent cell centre reconstruction
 509 of $\rho \mathbf{u}$ from surrounding values of V_f :

$$(\rho \mathbf{u})_C = \left(\sum_{f' \in c} \mathbf{d}_{f'} \otimes \mathbf{d}_{f'}^T \right)^{-1} \sum_{f' \in c} \mathbf{d}_{f'} V_{f'}$$

510 where $\mathbf{d}_{f'} \otimes \mathbf{d}_{f'}^T$ is a 3×3 tensor and so the inversion of the tensor sum is a local operation which
 511 can be calculated once for every cell in the grid before time-stepping begins. The H implied
 512 by this reconstruction of U is likely to be positive definite for meshes with sufficiently low non-
 513 orthogonality, although this has not been proved.

514 The semi-implicit technique involves combining the momentum 7a, continuity 7b and θ 7c
 515 equations and the equation of state 7d to form a Helmholtz equation to be solved implicitly, as
 516 described by Weller and Shahrokhi (2014). The semi-implicit solution technique with a Hodge
 517 operator can be defined by considering only a discretised form of the continuity equation:

$$\frac{\phi^{(n+1)} - \rho^{(n)}}{\Delta t} + \frac{1}{2} \left\{ \nabla \cdot (HV)^{(n)} + \nabla \cdot (HV)^{(n+1)} \right\} = 0. \quad (34)$$

518 The divergence is discretised using Gauss' divergence theorem so that:

$$\nabla \cdot (HV) = \frac{1}{\mathcal{V}_c} \sum_{f \in c} n_f (HV)_f \quad (35)$$

519 where \mathcal{V}_c is the volume of cell c , $f \in c$ denotes the faces of cell c , and $n_f = 1$ if \mathbf{d}_f points out-
 520 wards from the cell and $n_f = -1$ otherwise. Equation 35 is now a sum over a sum since $(HV)_f$
 521 is one element of a matrix-vector multiply. In order to simplify the construction of the matrix
 522 for the Helmholtz problem, only the diagonal terms of HV are treated implicitly. Therefore, H is
 523 separated into a diagonal and off-diagonal matrix:

$$H = H_d + H_{off}. \quad (36)$$

524 Equation 34 can now be approximated by:

$$\frac{\phi^{(n+1)} - \rho^{(n)}}{\Delta t} + \frac{1}{2} \left\{ \nabla \cdot (HV)^{(n)} + \nabla \cdot (H_d V)^{(n+1)} + \nabla \cdot (H_{off} V)^\ell \right\} = 0 \quad (37)$$

525 where superscript ℓ denotes lagged values taken from a previous iteration or from a previous stage
 526 of a Runge-Kutta scheme. This was the approach taken by Weller and Shahrokhi (2014). How-
 527 ever, the numerical solution of equation 37 turns out to be unstable when using a large time-step on
 528 highly non-orthogonal meshes associated with terrain following layers over steep orography. Im-
 529 proved stability and energy conservation can be achieved by splitting H into a diagonal component
 530 which would be correct on an orthogonal grid and a non-orthogonal correction:

$$H = H_c + H_{corr} \quad (38)$$

531 where the diagonal matrix $H_c = |\mathbf{S}_f|/|\mathbf{d}_f|$ and the non-orthogonal correction is $H_{corr} = H - H_c$.
 532 The orthogonal part, H_c , can be treated implicitly in the Helmholtz equation:

$$\frac{\phi^{(n+1)} - \rho^{(n)}}{\Delta t} + \frac{1}{2} \left\{ \nabla \cdot (HV)^{(n)} + \nabla \cdot (H_c V)^{(n+1)} + \nabla \cdot (H_{corr} V)^\ell \right\} = 0. \quad (39)$$

533 This form is used for the solutions of the Euler equations in this paper and is stable, with good
 534 energy conservation for all of the tests presented.

535 References

- 536 Adcroft, A., C. Hill, and J. Marshall, 1997: Representation of topography by shaved cells in a
 537 height coordinate ocean model. *Mon. Wea. Rev.*, **125**, 2293–2315.
- 538 Fast, J. D., 2003: Forecasts of valley circulations using the terrain-following and step-mountain
 539 vertical coordinates in the Meso-Eta model. *Wea. Forecasting*, **18**, 1192–1206.
- 540 Gal-Chen, T., and R. C. Somerville, 1975: On the use of a coordinate transformation for the
 541 solution of the navier-stokes equations. *J. Comp. Phys.*, **17**, 209–228.
- 542 Gallus, W. A., and J. B. Klemp, 2000: Behavior of flow over step orography. *Mon. Wea. Rev.*, **128**,
 543 1153–1164.

- 544 Gary, J. M., 1973: Estimate of truncation error in transformed coordinate, primitive equation
atmospheric models. *J. Atmos. Sci.*, **30**, 223–233.
- 545
- 546 Good, B., A. Gadian, S.-J. Lock, and A. Ross, 2014: Performance of the cut-cell method of
representing orography in idealized simulations. *Atmos. Sci. Lett.*, **15**, 44–49.
- 547
- 548 Jebens, S., O. Knoth, and R. Weiner, 2011: Partially implicit peer methods for the compressible
Euler equations. *J. Comp. Phys.*, **230**, 4955–4974.
- 549
- 550 Klein, R., K. Bates, and N. Nikiforakis, 2009: Well-balanced compressible cut-cell simulation of
atmospheric flow. *Philos. Trans. Roy. Soc. London*, **367**, 4559–4575.
- 551
- 552 Klemp, J. B., 2011: A terrain-following coordinate with smoothed coordinate surfaces. *Mon. Wea.
Rev.*, **139**, 2163–2169.
- 553
- 554 Leuenberger, D., M. Koller, O. Fuhrer, and C. Schär, 2010: A generalization of the SLEVE vertical
coordinate. *Mon. Wea. Rev.*, **138**, 3683–3689.
- 555
- 556 Melvin, T., M. Dubal, N. Wood, A. Staniforth, and M. Zerroukat, 2010: An inherently mass-
conserving iterative semi-implicit semi-lagrangian discretization of the non-hydrostatic vertical-
slice equations. *Quart. J. Roy. Meteor. Soc.*, **136**, 799–814.
- 557
- 558
- 559 Mesinger, F., Z. I. Janjić, S. Ničkovic, D. Gavrilov, and D. G. Deaven, 1988: The step-mountain
coordinate: Model description and performance for cases of alpine lee cyclogenesis and for a
560 case of an appalachian redevelopment. *Mon. Wea. Rev.*, **116**, 1493–1518.
- 561
- 562 Mesinger, F., and Coauthors, 2012: An upgraded version of the Eta model. *Meteor. Atmos. Phys.*,
116, 63–79.
- 563
- 564 OpenCFD Foundation, cited 2015: OpenFOAM® – User Guide. [Available online at [http://cfd.
direct/openfoam/user-guide/snappyhexmesh/#x26-1510005.4](http://cfd.direct/openfoam/user-guide/snappyhexmesh/#x26-1510005.4)].
- 565

- 566 Schär, C., D. Leuenberger, O. Fuhrer, D. Lüthi, and C. Girard, 2002: A new terrain-following
567 vertical coordinate formulation for atmospheric prediction models. *Mon. Wea. Rev.*, **130**, 2459–
568 2480.
- 569 Simon, J. S., K. A. Lundquist, and F. K. Chow, 2012: Application of the immersed boundary
570 method to simulations of flow over steep, mountainous terrain. *15th Conf. on Mountain Met.*,
571 Steamboat, CO.
- 572 Steppeler, J., H.-W. Bitzer, M. Minotte, and L. Bonaventura, 2002: Nonhydrostatic atmospheric
573 modeling using a z -coordinate representation. *Mon. Wea. Rev.*, **130**, 2143–2149.
- 574 Steppeler, J., R. Hess, U. Schättler, and L. Bonaventura, 2003: Review of numerical methods for
575 nonhydrostatic weather prediction models. *Meteor. Atmos. Phys.*, **82**, 287–301.
- 576 Steppeler, J., S.-H. Park, and A. Dobler, 2013: Forecasts covering one month using a cut-cell
577 model. *Geosci. Model Dev.*, **6**, 875–882.
- 578 Thuburn, J., and C. Cotter, 2012: A framework for mimetic discretization of the rotating shallow-
579 water equations on arbitrary polygonal grids. *SIAM J. Sci. Comp.*, **34** (3), B203–B225.
- 580 Webster, S., A. Brown, D. Cameron, and C. Jones, 2003: Improvements to the representation of
581 orography in the met office unified model. *Quart. J. Roy. Meteor. Soc.*, **129**, 1989–2010.
- 582 Weller, H., and A. Shahrokhi, 2014: Curl free pressure gradients over orography in a solution of
583 the fully compressible Euler equations with implicit treatment of acoustic and gravity waves.
584 *Mon. Wea. Rev.*, **142**, 4439–4457.
- 585 Yamazaki, H., and T. Satomura, 2010: Nonhydrostatic atmospheric modeling using a combined
586 Cartesian grid. *Mon. Wea. Rev.*, **138**, 3932–3945.

- 587 Zängl, G., 2012: Extending the numerical stability limit of terrain-following coordinate models
- 588 over steep slopes. *Mon. Wea. Rev.*, **140**, 3722–3733.

589 **LIST OF TABLES**

590 Table 1.	Minimum and maximum tracer magnitudes and ℓ_2 error norms (defined by 591 equation 13) at $t = 10000$ s in the horizontal and terrain following tracer ad- 592 vection tests using centred linear and cubic upwind-biased schemes. For the 593 horizontal advection test, ℓ_2 error norms, minimum and maximum values are 594 given for the fourth order scheme using the modified code from Schär et al. 595 (2002).	32
596 Table 2.	Spatial and temporal resolutions used in the gravity waves test. The resolution 597 of $\Delta z = 300$ m has the same parameters as the original test case specified by 598 Schär et al. (2002). At other resolutions, the vertical resolution is prescribed, 599 and horizontal and temporal resolutions are calculated to preserve the same 600 aspect ratio as the original test case.	33
601 Table 3.	Cell area ratios and nonorthogonality of BTF and cut cell grids used in the 602 gravity waves and thermal advection tests. Cell sizes are almost uniform on 603 BTF grids, but for the cut cell grids the cell area ratio gives an indication of the 604 smallest cell sizes. Nonorthogonality is the angle between the surface normal 605 vector and the vector joining the two adjacent cell centres. Except at coarse 606 resolutions, cut cell grids have greater maximum nonorthogonality than BTF 607 grids.	34

TABLE 1. Minimum and maximum tracer magnitudes and ℓ_2 error norms (defined by equation 13) at $t = 10000$ s in the horizontal and terrain following tracer advection tests using centred linear and cubic upwind-biased schemes. For the horizontal advection test, ℓ_2 error norms, minimum and maximum values are given for the fourth order scheme using the modified code from Schär et al. (2002).

			Analytic	BTF	SLEVE	Cut cell	No terrain
Horizontal	Centred linear	ℓ_2 error	0	0.284	0.0316	0.0304	0.0304
		min	0	-0.275	-0.0252	-0.0251	-0.0251
		max	1	0.925	0.985	0.985	0.985
	Fourth order	ℓ_2 error	0	0.0938	0.00244	—	0.00234
		min	0	-0.0926	-0.00174	—	-0.00178
		max	1	1.00	0.984	—	0.983
Terrain following	Centred linear	ℓ_2 error	0	0.112	0.0146	0.00784	0.00784
		min	0	-0.0464	-0.0106	-0.000674	-0.00674
		max	1	0.922	0.982	0.983	0.983
	Cubic upwind-biased	ℓ_2 error	0	0.0341	0.235	unstable	—
		min	0	-0.0245	-0.120	unstable	—
		max	1	0.985	0.950	unstable	—
	Cubic upwind-biased	ℓ_2 error	0	0.0209	0.162	0.181	—
		min	0	-0.0110	-0.0263	-0.0284	—
		max	1	0.983	0.865	0.851	—

612 TABLE 2. Spatial and temporal resolutions used in the gravity waves test. The resolution of $\Delta z = 300\text{ m}$ has
 613 the same parameters as the original test case specified by Schär et al. (2002). At other resolutions, the vertical
 614 resolution is prescribed, and horizontal and temporal resolutions are calculated to preserve the same aspect ratio
 615 as the original test case.

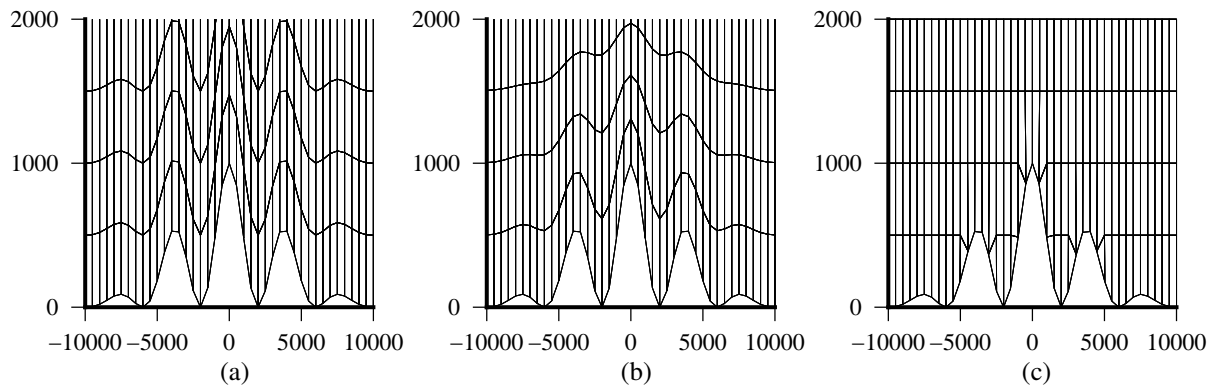
Δz (m)	Δx (m)	Δt (s)
500	833.3	13.33
300	500	8
250	416.7	6.667
200	333.3	5.333
150	250	4
125	208.3	3.333
100	166.7	2.667
75	125	2
50	83.33	1.333

616 TABLE 3. Cell area ratios and nonorthogonality of BTF and cut cell grids used in the gravity waves and
 617 thermal advection tests. Cell sizes are almost uniform on BTF grids, but for the cut cell grids the cell area ratio
 618 gives an indication of the smallest cell sizes. Nonorthogonality is the angle between the surface normal vector
 619 and the vector joining the two adjacent cell centres. Except at coarse resolutions, cut cell grids have greater
 620 maximum nonorthogonality than BTF grids.

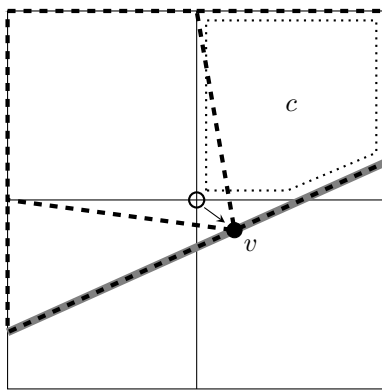
Δz (m)	max/min cell area ratio		Maximum nonorthogonality ($^{\circ}$)	
	BTF	Cut cell	BTF	Cut cell
500	1.01	1.68	9.2	4.1
300	1.01	4.33	10.2	7.3
250	1.01	5.42	10.8	20.9
200	1.01	25.4	10.8	31.9
150	1.01	10.0	11.0	29.4
125	1.01	10.1	11.1	24.37
100	1.01	36.3	11.1	32.2
75	1.01	52.9	11.2	34.2
50	1.01	75.3	11.2	31.7

621 LIST OF FIGURES

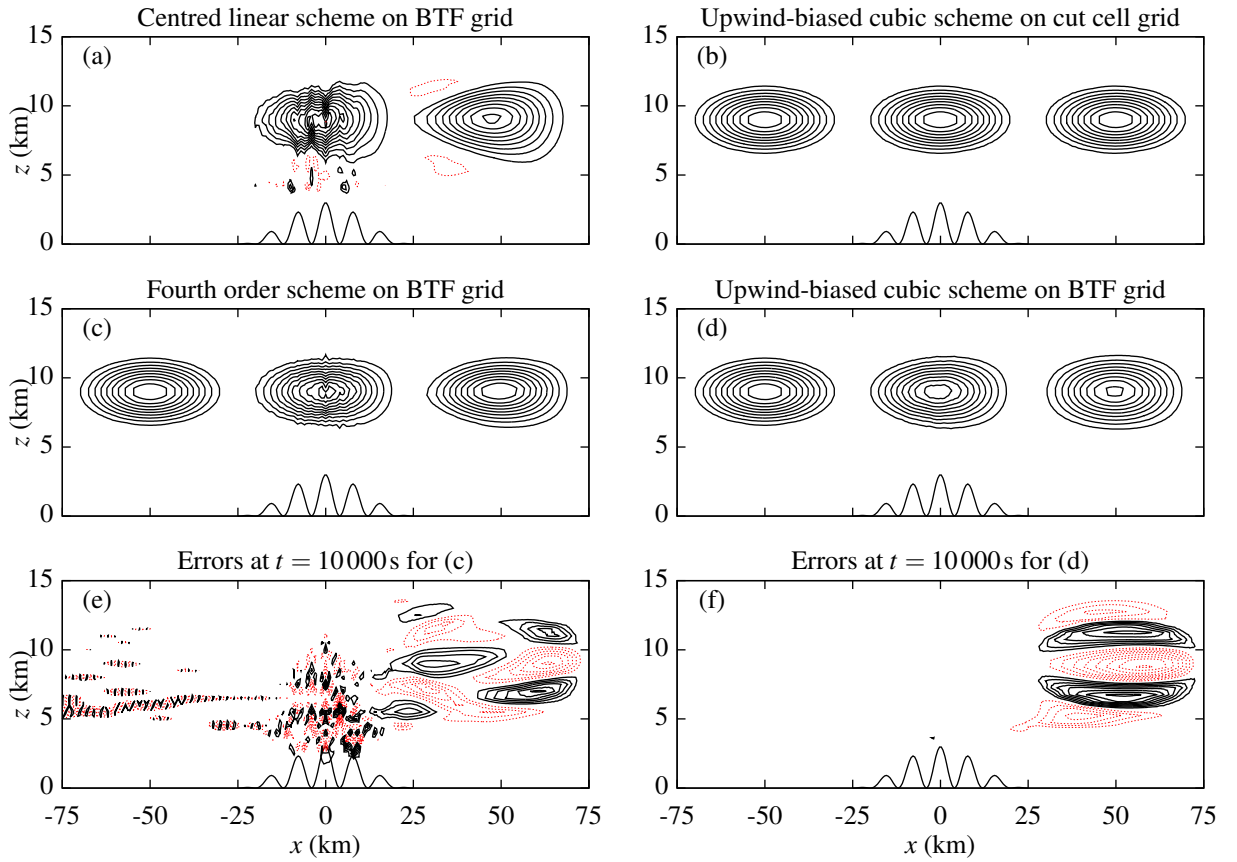
622	Fig. 1.	Examples of (a) BTF, (b) SLEVE, and (c) a cut cell grid, showing cell edges in the lowest 623 four layers. The full two dimensional grids are 20 km wide and 20 km high. SLEVE param- 624 eters are specified in the resting atmosphere test in section 4c. The cut cell grid was created 625 by intersecting the terrain surface with a regular grid as described in section 2. Axes are in 626 units of m.	36
627	Fig. 2.	Illustrative behaviour of the <code>snappyHexMesh</code> tool in cut cell grid creation. The terrain 628 surface, denoted by a thick grey line, is taken from the lower boundary of the BTF grid. The 629 surface is intersected with a rectangular grid shown by thin solid lines. Vertex v is ‘snapped’ 630 to the surface, moving from the position marked by the open circle to that of the closed 631 circle. The resultant cut cell grid is shown by thick dashed lines. With a typical cut cell 632 technique, cell c would be a pentagon, as shown by the dotted line, but <code>snappyHexMesh</code> 633 produces a quadrangular cell.	37
634	Fig. 3.	Horizontally advected tracer contours at $t = 0$ s, 5000 s and 10 000 s using (a) centred linear 635 scheme on the BTF grid, (b) the upwind-biased cubic scheme on the cut cell grid, (c) the 636 fourth order scheme from Schär et al. (2002) on the BTF grid, and (d) the upwind-biased 637 cubic scheme on the BTF grid with contour intervals every 0.1. Errors on the BTF grid at 638 $t = 10 000$ s are shown for (e) the fourth order scheme from Schär et al. (2002), and (f) the 639 upwind-biased cubic scheme, with contour intervals every 0.01. Negative contours denoted 640 by dotted lines. The terrain profile is also shown immediately above the x axis. Subfigures 641 (c) and (e) produced using the modified version of the code from Schär et al. (2002).	38
642	Fig. 4.	Maximum spurious vertical velocity, w (m s^{-1}), in the resting atmosphere test with results on 643 BTF, SLEVE, cut cell and regular grids using the model from Weller and Shahrokhi (2014) 644 which includes a curl-free pressure gradient formulation.	39
645	Fig. 5.	Cut cell grids used for the gravity waves and thermal advection tests at (a) $\Delta z = 300$ m, (b) 646 $\Delta z = 250$ m, and (c) $\Delta z = 200$ m. The mountain peak $h_0 = 250$ m. At $\Delta z = 250$ m, the grid 647 creation process has merged small cells with the cells in the layer above but, at $\Delta z = 200$ m, 648 small cells have been retained. The full two dimensional grids are 300 km wide and 30 km 649 high. Axes are in units of m.	40
650	Fig. 6.	Differences in potential temperature between the start and end of the gravity waves test on 651 the BTF grid with $\Delta z = 50$ m. The dashed line at $x = 50$ km marks the position of the vertical 652 profile in figure 7. Axes are in units of m.	41
653	Fig. 7.	Vertical profiles of potential temperature differences between the start and end of the gravity 654 waves test on (a) the BTF grid, and (b) the cut cell grid. Results are compared with thermal 655 advection tests results, showing differences in tracer density between the numeric and ana- 656 lytic solutions at $t = 18 000$ s on (c) the BTF grid, and (d) the cut cell grid. The results are 657 convergent, with the exception of the cut cell grid at $\Delta z = 500$ m, and errors are found in the 658 lowest layers on the cut cell grids.	42
659	Fig. 8.	Error in tracer density in the thermal advection test at a resolution of $\Delta z = 50$ m on (a) the 660 BTF grid, and (b) the cut cell grid. Errors are negligible on the BTF grid, but on the cut cell 661 grid errors are generated near mountainous terrain and are advected horizontally on the lee 662 side. Axes are in units of m.	43



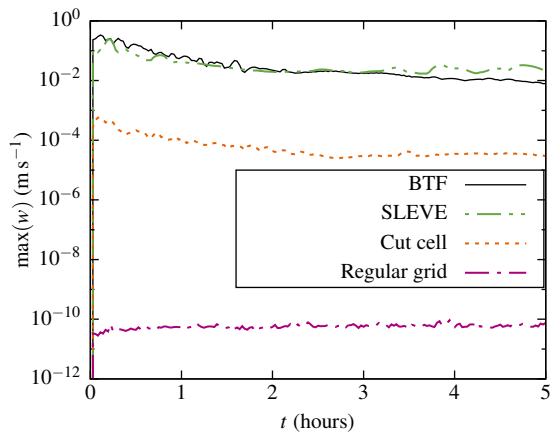
663 FIG. 1. Examples of (a) BTF, (b) SLEVE, and (c) a cut cell grid, showing cell edges in the lowest four layers.
 664 The full two dimensional grids are 20 km wide and 20 km high. SLEVE parameters are specified in the resting
 665 atmosphere test in section 4c. The cut cell grid was created by intersecting the terrain surface with a regular grid
 666 as described in section 2. Axes are in units of m.



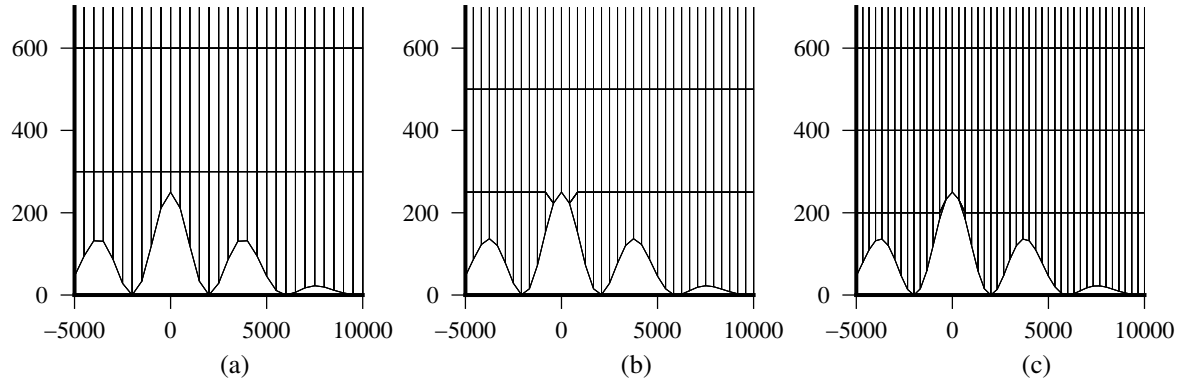
667 FIG. 2. Illustrative behaviour of the `snappyHexMesh` tool in cut cell grid creation. The terrain surface,
 668 denoted by a thick grey line, is taken from the lower boundary of the BTF grid. The surface is intersected with
 669 a rectangular grid shown by thin solid lines. Vertex v is ‘snapped’ to the surface, moving from the position
 670 marked by the open circle to that of the closed circle. The resultant cut cell grid is shown by thick dashed lines.
 671 With a typical cut cell technique, cell c would be a pentagon, as shown by the dotted line, but `snappyHexMesh`
 672 produces a quadrangular cell.



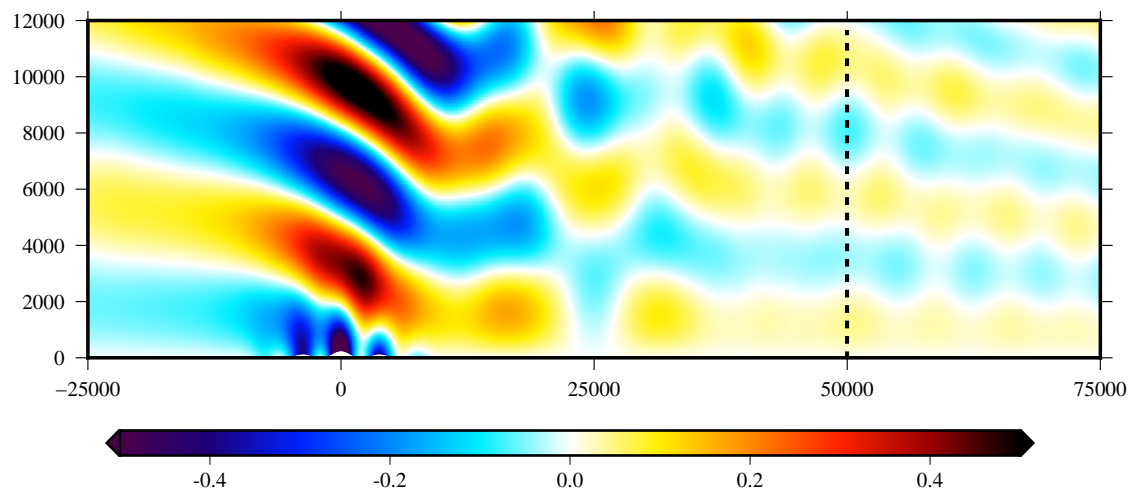
673 FIG. 3. Horizontally advected tracer contours at $t = 0$ s, 5000 s and 10000 s using (a) centred linear scheme on
 674 the BTF grid, (b) the upwind-biased cubic scheme on the cut cell grid, (c) the fourth order scheme from Schär
 675 et al. (2002) on the BTF grid, and (d) the upwind-biased cubic scheme on the BTF grid with contour intervals
 676 every 0.1. Errors on the BTF grid at $t = 10000$ s are shown for (e) the fourth order scheme from Schär et al.
 677 (2002), and (f) the upwind-biased cubic scheme, with contour intervals every 0.01. Negative contours denoted
 678 by dotted lines. The terrain profile is also shown immediately above the x axis. Subfigures (c) and (e) produced
 679 using the modified version of the code from Schär et al. (2002).



680 FIG. 4. Maximum spurious vertical velocity, w (m s^{-1}), in the resting atmosphere test with results on BTF,
 681 SLEVE, cut cell and regular grids using the model from Weller and Shahrokhi (2014) which includes a curl-free
 682 pressure gradient formulation.



683 FIG. 5. Cut cell grids used for the gravity waves and thermal advection tests at (a) $\Delta z = 300$ m, (b) $\Delta z = 250$ m,
 684 and (c) $\Delta z = 200$ m. The mountain peak $h_0 = 250$ m. At $\Delta z = 250$ m, the grid creation process has merged small
 685 cells with the cells in the layer above but, at $\Delta z = 200$ m, small cells have been retained. The full two dimensional
 686 grids are 300 km wide and 30 km high. Axes are in units of m.



687 FIG. 6. Differences in potential temperature between the start and end of the gravity waves test on the BTF
 688 grid with $\Delta z = 50$ m. The dashed line at $x = 50$ km marks the position of the vertical profile in figure 7. Axes are
 689 in units of m.

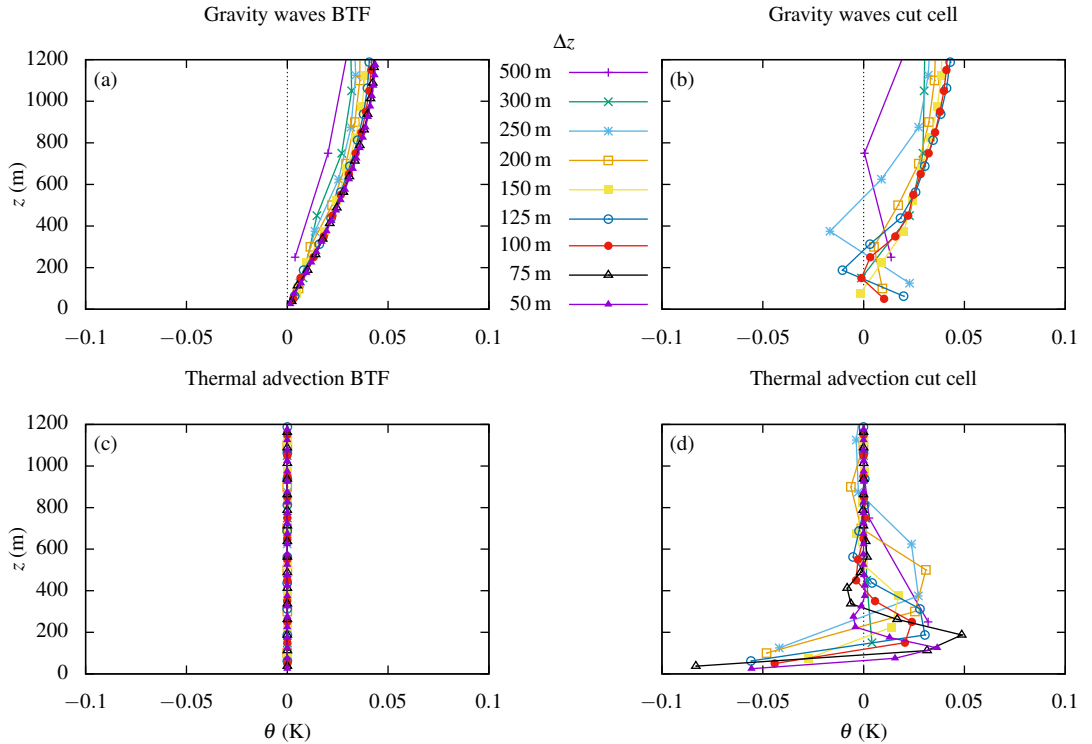
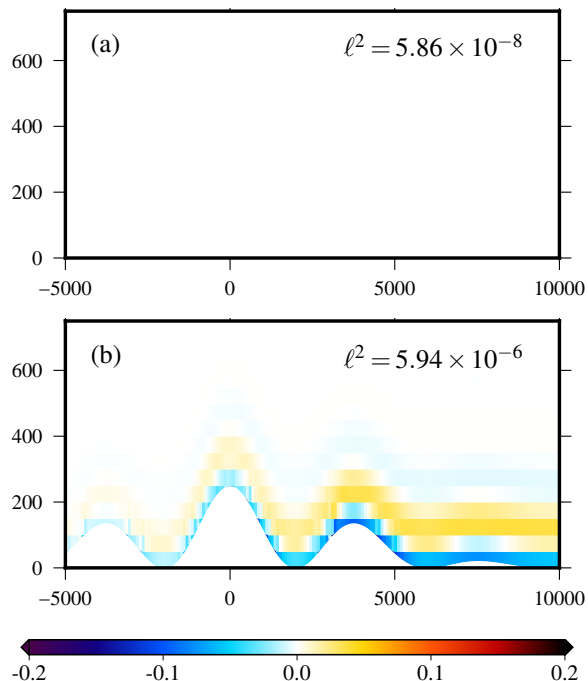


FIG. 7. Vertical profiles of potential temperature differences between the start and end of the gravity waves test on (a) the BTF grid, and (b) the cut cell grid. Results are compared with thermal advection tests results, showing differences in tracer density between the numeric and analytic solutions at $t = 18000$ s on (c) the BTF grid, and (d) the cut cell grid. The results are convergent, with the exception of the cut cell grid at $\Delta z = 500$ m, and errors are found in the lowest layers on the cut cell grids.



695 FIG. 8. Error in tracer density in the thermal advection test at a resolution of $\Delta z = 50\text{ m}$ on (a) the BTF grid,
 696 and (b) the cut cell grid. Errors are negligible on the BTF grid, but on the cut cell grid errors are generated near
 697 mountainous terrain and are advected horizontally on the lee side. Axes are in units of m.